Two-photon lithography for dielectric structures and electroplating molds for retinal prostheses

Tiffany W Huang, Charles Z. Chen, Jack Andraka, and David Heydari
Staff mentor: Swaroop Kommera, External mentors: Palanker lab

I. Introduction and Motivation

a) Retinal prostheses

Retinal degenerative diseases, such as age-related macular degeneration and retinitis pigmentosa, lead to blindness due to a gradual loss of photoreceptors [1, 2]. Retinal prostheses aim to restore sight in patients suffering from these conditions via electrical stimulation of the surviving inner retinal neurons [3]. In the epiretinal approach, the primary target of stimulation are the retinal ganglion cells (RGCs), while subretinal stimulation elicits visual responses via inner retinal neurons (primarily bipolar cells). Both of these configurations have been approved for clinical use; however, current retinal prostheses systems employ bulky implanted electronics with trans-scleral cables that necessitate complex and risky surgical procedures [4-7]. In addition, visual acuity with the Argus II epiretinal system is limited with percept distortion due to axonal stimulation [8].

To improve on these visual acuity levels, the Palankar lab has developed an alternative approach to retinal prostheses predicated on a photovoltaic subretinal pixel array directly converting pulsed light into electrical signals. The energy and information of the signal are delivered to the implant via projected image, eliminating the need for trans-scleral cables and greatly simplifying the accompanying surgical procedures for implantation of the prostheses. Each pixel in the photovoltaic array is composed of a central stimulating electrode and a peripheral return electrode connected to the photodiode. Photocurrent generated in the diodes flows through the tissue via electrodes coated in sputtered iridium oxide (SIROF).

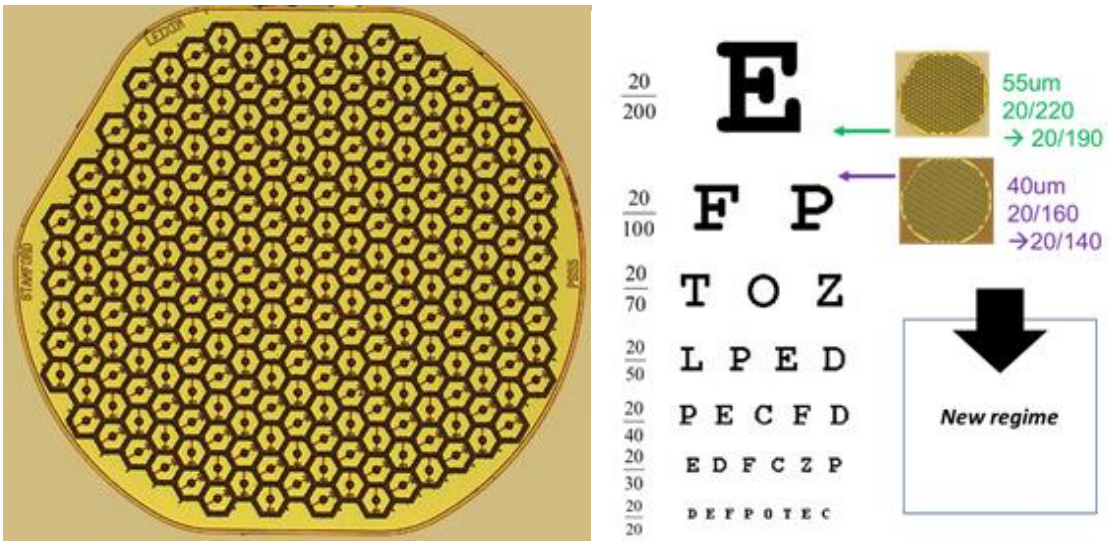

Figure 1 (a) 55um-wide pixel array, with two photodiodes in each pixel. **(b)** Relationship between pixel size and visual acuity.

The resulting electric field in the retina polarizes nearby neurons, leading to their stimulation. Previous iterations of this prostheses employed 70 um-wide and 30 um-thick pixels separated by 5 um trenches and arranged in a hexagonal pattern over a 1mm diameter chip (142 pixels). Local return electrodes in each pixel provide greater spatial confinement of the electric field compared to monopolar arrays such as the Alpha IMS [5], thus yielding higher contrast of detected patterns [5]. However, these 70 um-wide pixels are limited to a visual acuity of 20/260, essentially because the pixels are too large to achieve any better performance. The legal blindness standard in the United States is 20/200. To achieve higher visual acuity, there is no other way but to proceed with smaller pixel size. Palanker Lab has fabricated new-generation devices with 55um- and 40um-wide respectively. With 55um-wide pixels, subretinal pixel array is predicted to be capable for 20/200 vision restoration.

However, a critical issue of decreasing pixel size is that the stimulation threshold increases because of the dispersion of electric field. With the same stimulation voltage, the shape of the potential field emanating from a pixel scales proportionally to the size of the pixel. Smaller pixel size thus causes more shallow penetration of electric field into the inner nuclear layer for an equivalent voltage. To achieve stimulation of the inner nuclear layer, smaller pixels would require a higher voltage, often exceeding the water window, making them ill-suited an implanted device. Furthermore, smaller size pixels introduce more cross-talk between neighboring pixels, which further compromises the performance of subretinal prosthesis.

To address these shortcomings, we pursued the construction of 3D honeycomb walls around each pixel to confine the electric field to the vertical direction. Comsol simulation shows that building dielectric walls significantly increases the vertical penetration of electric field in saline water, while even better confinement is provided by a metal structure. Cross-talk is also minimized. Therefore, using Nanoscribe, a two-photon lithography tool, we aimed to build (1) polymer honeycomb structures on our current planar 55um-pixel arrays, with negative photoresist; (2) Electroplating molds for future fabrication of metal honeycomb walls, using positive photoresist.

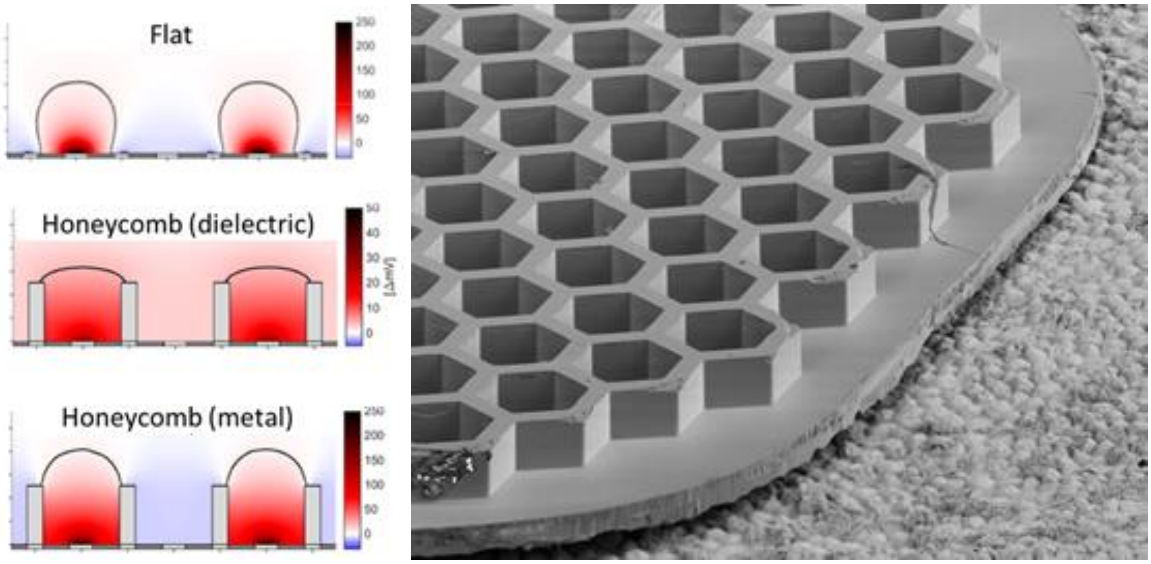

Figure 2 (a) Comsol simulations of electric field for planar electrodes, and dielectric and metal walls. **(b)** 55 um diameter honeycomb pixels made in silicon. (Note: This is not a real device, but rather a silicon model)

b) Two-Photon Lithography

Two-photon polymerization (TPP) is a powerful technology that has been utilized extensively for the fabrication of true three-dimensional (3D) micro/nanostructures of various materials with sub diffraction-limit resolution [9]. TPP is a photochemical process initiated by a femtosecond laser beam focused tightly by a high-numerical-aperture (NA) objective into the volume of a photosensitive resins. A normal TPP process is described in equations (1), (2), and (3). Akin to free radical polymerization, it consists of three processes, the initiation process, the propagation process, and the termination process [10]. In the initiation process, photoinitiators (PIs) reach their excited state (PI*) by absorption of two photons and decompose to radicals (R·). In the propagation process, the radicals combine with monomers (M) to produce monomer radicals ($RM_n\cdot$). In the termination process, two monomer radicals are combined and the photo-polymerization process is terminated.

$$PI \xrightarrow{hv+hv} PI^* \rightarrow R\cdot + R\cdot \quad (1)$$

$$R\cdot + M \rightarrow RM\cdot \xrightarrow{M} RMM\cdot \ldots \rightarrow RM_n\cdot \quad (2)$$

$$RM_n\cdot + RM_m\cdot \rightarrow RM_{n+m}R \quad (3)$$

Two-photon absorption (TPA) is the fundamental process of TPP and it is one of the multiphoton absorption (MPA) processes. In contrast to one-photon absorption (OPA), the TPA process involves PIs absorbing two photons simultaneously when the initiator molecule transits from a lower energy level to a higher energy level, thus resulting in the subtraction of two energy levels. This absorption reaction is a third-order nonlinear optical process [11], with the absorption rate of energy being proportional to the square of light intensity, which is expressed as:

$$\frac{dW}{dt} = \frac{8\pi^2\omega}{n^2c^2} I^2 Im(\chi^{(3)})$$

Where n is the refractive index, ω is the incident light optical frequency, c is the speed of light in vacuum, I is the intensity of the light, and $Im(\chi^{(3)})$ is the imaginary part of the third-order susceptibility. As a result, the polymerization reaction is effectively confined to the focal point of the laser, resulting in a reduced cross section which necessitates an ultra-short pulse laser with high intensities for precision patterning [12]. Additionally, the polymerization process ideally proceeds when the concentration of radicals exceeds a certain threshold due to radical quenchers in the resin. Thus, there is a threshold of laser intensity when irradiation time at a certain laser intensity initiates the photopolymerization reaction in a patterned area (See Figure 3). However, we note that the polymerization chain reaction can also occur via avalanche ionization under high intensity illumination [13].

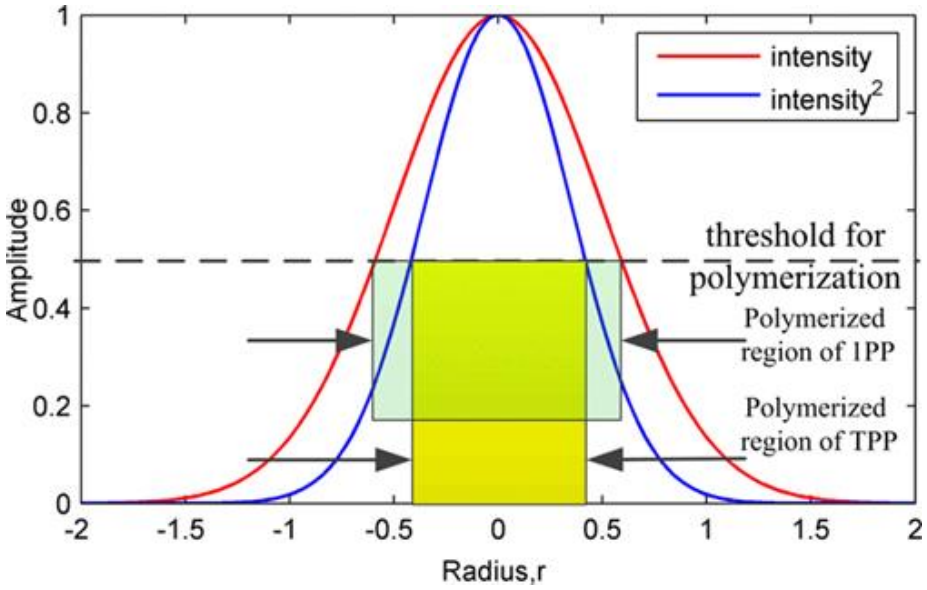

Figure 3. Distribution of light intensity in the laser focus of a Gaussian beam: where the beam waist is $w_0 = 1$ and the light intensity at the focus is $I_0 = 1$(dimensionless for clarity). The intensity (red) and the squared intensity (blue) are plotted. Photopolymerization processes take place at the region where light intensity reaches the threshold for polymerization. Thus, the polymerized region of TPP is smaller than that of OPP [9].

3D Direct Laser Writing with TPP

Three-dimensional direct laser writing (DLW), also known as 3D photolithography, is a powerful tool in which the TPP process is employed in the production of 3D micro- or nanostructures directly inside a material, usually a photoresist [14]. The technique consists of a femtosecond pulsed laser being tightly focused via a high-NA objective inside a photoresist with the laser operating at a wavelength at which the photoresist is transparent. Using TPP, the chemical and physical properties of the photoresist are altered within a small volume that is constrained by the irradiated laser intensity. Generally, this volume pixel is called a “voxel” and is commonly in the shape of an ellipsoid, enabling the fabrication of 2D and 3D structures with high resolution and arbitrary shape [15]. The unexposed parts of the photoresist are subsequently washed away in the developer bath, leaving a free-standing 3D structure.

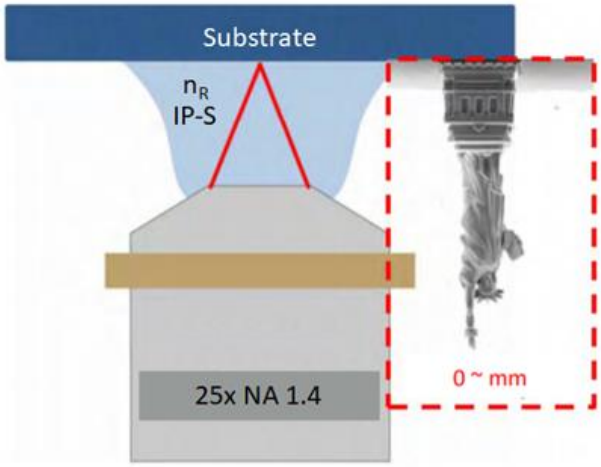

Figure 4. Scheme of regular three-dimensional direct-laser writing optical lithography [14]

TPP Patterning System

The optical system for TPP varies according to different applications. For our purposes, we employed the commercial two-photon DLW system by Nanoscribe GmbH [16]. In this system, a pulsed erbium doped femtosecond fiber laser is used with center wavelength calibrated to 780 nm. The pulse duration is approximately 100 fs and a repetition rate of approximately 80 MHz. The peak power is 25 kW with an average output power <180 mW [l7] The femtosecond pulses generated by this laser are then focused onto the substrate via a high NA objective (we use the 25x NA = 0.8 objective).

A CMOS camera enables real-time process monitoring. The 3D scanning of the laser beam relative to the sample for DLW is realized along three registers. First an xy-stage controlled by a 3D linear motor-driven stage enables the handling of multiple different substrate chips and writing positions on a single substrate. This is subsequently combined with a 3D piezoelectric (PZT) stage, that travels with the xy-stage (installed on top of the xy-stage) and enables high resolution patterning, but with limited travel and scanning speed. Lastly, a two-dimensional (xy) galvanometer is combined with this system to rapidly fabricate microstructures over large areas when combined with the xy-stage (mm-scale coverage). Our research primarily focuses on the galvanometer and xy-stage patterning regime owing to its rapid speed high resolution, and wide coverage area.

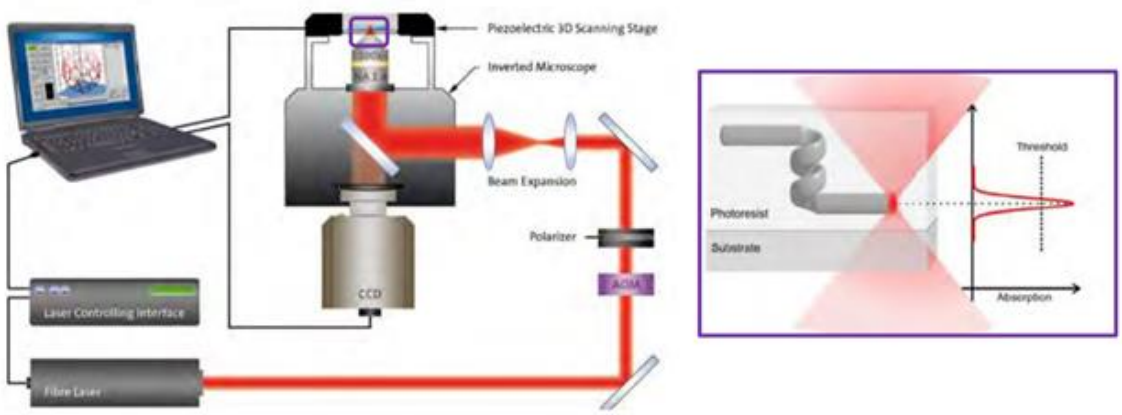

Figure 5. Experimental setup of Nanoscribe DLW system [1]

c) **TPP Patterning System parameters**

The Nanoscribe GmbH system has many tunable parameters. These include the laser power, the slicing distance, the hatching distance, interface position, and block size for large structures. Hatching distance sets the distance between lines scanned in the xy-plane, and the slicing distance sets the distance between lines scanned in the z-plane. The interface position is defined as the distance below the interface at which the laser starts writing the pattern, in order to ensure the pattern reaches the substrate bottom. Block size indicates the size of a write field. If a pattern is larger than the block size, the pattern is divided into blocks, and the stage is moved to address each block. Figure 6 depicts these parameters.

The dose required to polymerize a negative resist or clear a positive resist depends mainly on the number of photons accumulated in the focal spot. Dosage is roughly proportional to $\frac{laserpower^2}{scanspeed}$[17].

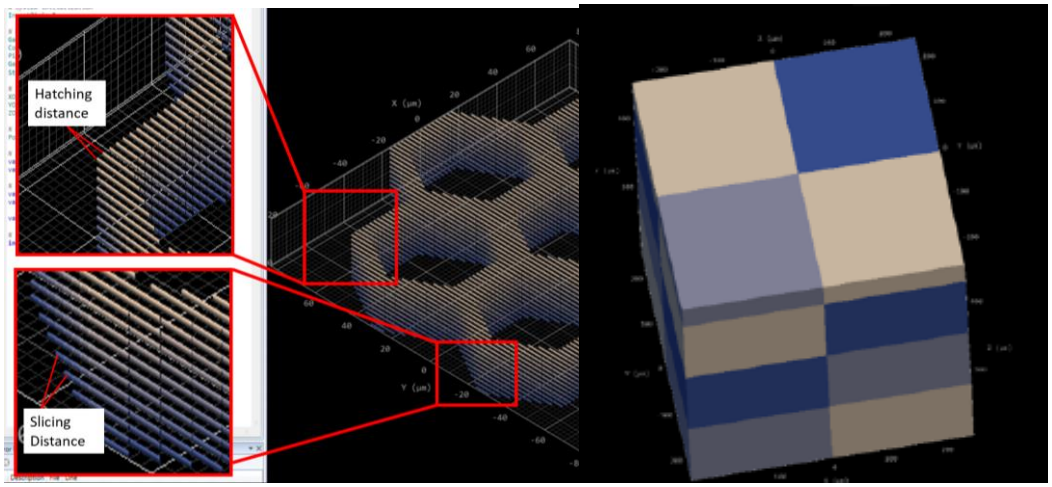

Figure 6. (a) Depictions of hatching distance and slicing distance on a hexagonal test structure. **(b)** Depictions of a cuboid broken into different blocks, by color [1].

II. Resist structures

a) Thermal "Bubbling" on SIROF

Nanoscribe fabrication of dielectric structures on these implants is different from standard Nanoscribe fabrication in two respects. Firstly, the implants are only 1mm in diameter and 30um thick and thus must be mounted to a larger substrate using a removable adhesive. Secondly, the implant surface consists of patterned sputtered iridium oxide (SIROF) and SiC rather than the more standard Si or quartz.

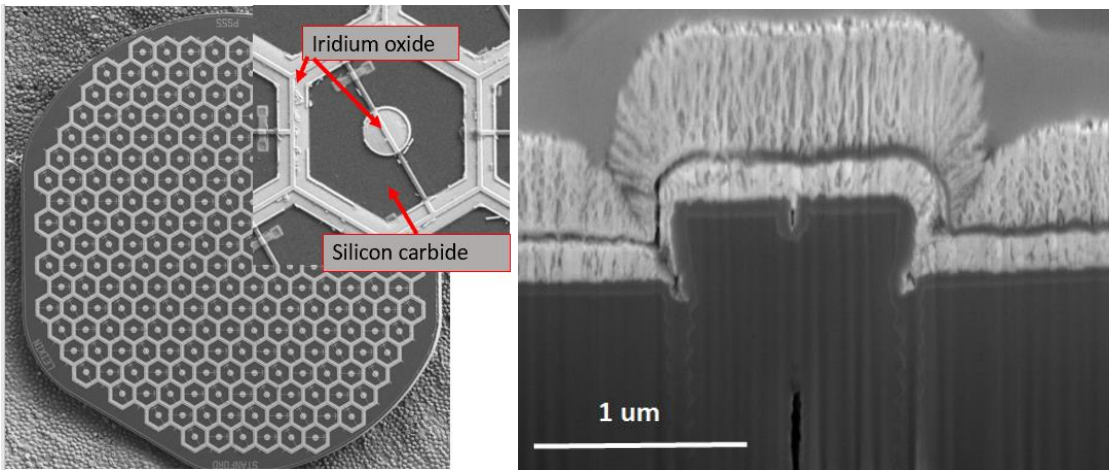

Figure 7. (a) Top-down image of a retinal prostheses implant and the exposed materials. SEM courtesy of Thomas Flores. **(b)** Cross-section of the iridium oxide hexagonal region. This cross section shows a trench which is filled with silicon dioxide and polysilicon, the titanium and platinum electrode, and the titanium and sputtered iridium oxide film (SIROF)

Fabricating resist structures involves a series of steps. First, the implant is mounted to a wafer substrate with a removable adhesive. Then, IP-S resist is drop-cast onto the device. The pattern is aligned to the patterned substrate in Nanoscribe. Then, the pattern is exposed. Next, the pattern is developed in 20 min of SU-8 developer. Finally, the adhesive is removed and the device is characterized by optical and scanning electron microscopy.

Initial exploration of fabricating the honeycomb resist structures on top of retinal prostheses showed 'bubbling' on the surfaces of the prostheses, particularly in the corners of hexagons. These bubbles, on the order of 10 um in diameter, affect the structural integrity of the resist structures and the ability of the structures to confine the electric field, necessitating a method to get rid of these 'bubbles.' We hypothesize that bubble formation is primarily a thermal effect, wherein enough heat accumulates to cause the resist to effectively boil. This is related to the underlying substrate, as bubbles do not appear when exposed with the same conditions on a silicon wafer.

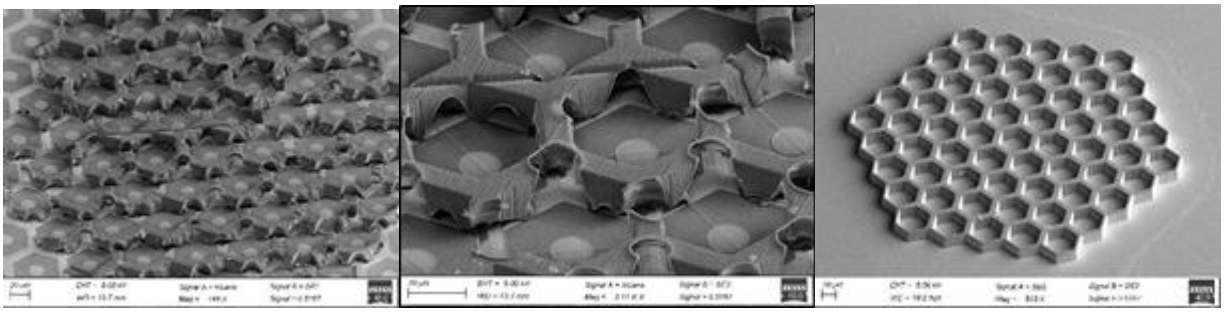

Figures 8. (a, b) 'Bubble' generation on resist structures formed atop retinal prostheses. **(c)** Resist structures atop a bare silicon wafer (SEMs courtesy of Thomas Flores).

While several papers study the formation of bubbles by femtosecond laser in solid materials [18-20], we have not come across a detailed discussion of bubble formation on polymers. Also, they maintain that mechanism for bubble formation and evolution needs further investigation [18]. Literature shows that extreme conditions with high temperature and pressure, intense physical and chemical changes such as boiling can occur [18]. Other works discussed the effect of thermal accumulation on the loss of fidelity in polymeric structures [13].

Our explanation of the extremely different behavior of bare silicon and SIROF surfaces is as follows:

I. Bare silicon surface is reflective to some extent, while SIROF surface is dark. From bare silicon to SIROF, **light absorption** dramatically increases. This would significantly lower the bubbling threshold (i.e., laser power with which bubbling effect reaches the level that prevents any complete structure to form.)

II. A **reflection** path should increase photon density near the interface. Because of lower reflectivity of SIROF, the polymerization threshold should be higher compare with bare silicon. This is confirmed in our communication with Nanoscribe technical support team.

III. Bare silicon has a much higher **thermal diffusivity** compared to the materials present in the retinal prostheses mounted on silicon. Silicon is on the order of $10^{-5}\ \frac{m^2}{s}$. Oxides have thermal diffusivities on the order of $10^{-7}\ \frac{m^2}{s}$.

b) Effect of adhesives

In light of the hypothesized thermal basis of the bubbling phenomenon, we decided to investigate the impact of the adhesive used to mount the devices on a larger silicon wafer in preparation for honeycomb structure fabrication. We hypothesize that the choice of the adhesive will dramatically impact the amount of polymer bubbling due to its role as a thermal insulator or conductor. Initially, devices were mounted to wafers using a nail polish formulation, which yielded tilted device mounts that made patterning of device-wide structures untenable while also producing widespread bubbling. Thus, two additional adhesives were explored for mounting the devices: polydimethylsiloxane (PDMS; 1:10 ratio of developer to base) and silver paint. For mounting devices, silver paint and nail polish were "smeared" onto the wafer using a small paint brush, after which the device was pressed into the still drying adhesive. For PDMS, the adhesive was spun coat onto the wafer at a speed of 2500 rpm, which yielded an adhesive thickness of 28 μm, after which the PDMS-coated wafer was baked overnight at 90°C. Devices were then pressed onto the cured PDMS layer, where they were held primarily by Van der Waals forces. Adhesives

were then evaluated on the basis of how flat the devices were (measured with an Alphastep 500 profilometer) and the amount of bubbling on the devices across the parameter space (see Figures 9 and 10 for summarized findings).

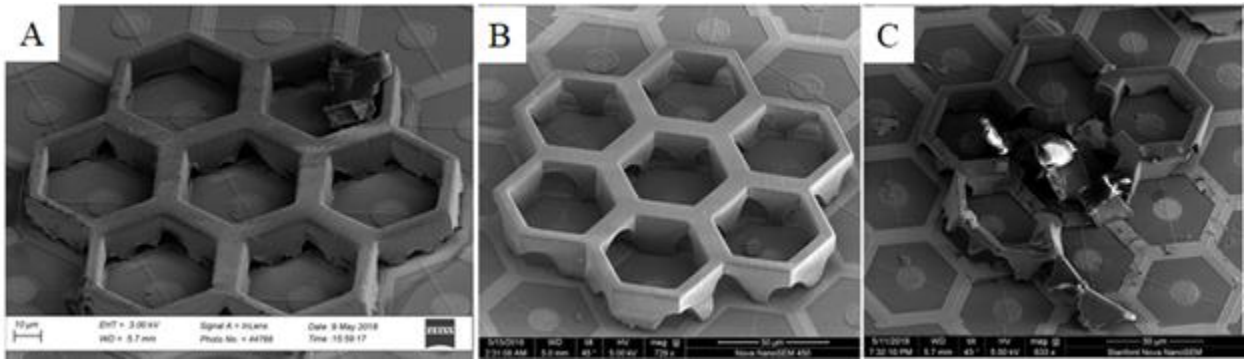

Figure 9. Impact of adhesive on bubbling at reduced Nanoscribe conditions (laser power = 30%, scanning speed = 2,500 um/s, hatching distance = 0.5 um, slicing distance = 1 um). As seen PDMS **(a)** has the least amount of bubbling in comparison to silver paint **(c)** and nail polish **(b)**.

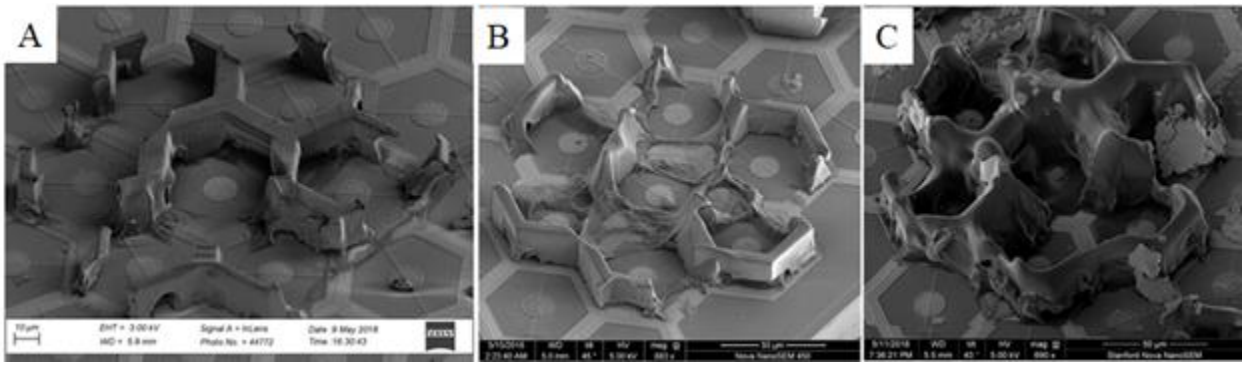

Figure 10. Impact of adhesive on bubbling at standard Nanoscribe conditions (laser power = 100%, scanning speed = 100,000 um/s, hatching distance = 0.3 um, slicing distance = 0.3 um). As seen PDMS **(a)** has comparable bubbling to silver paint **(c)** and less bubbling than nail polish **(b)**

As evidenced from these bubbling results, we can see that PDMS yielded the least amount or a comparable amount of bubbling in comparison to silver paint and nail polish, across the parameter space. Additionally, PDMS provided the highest consistency producing flat-mounted devices (insignificant slope vs. <0.5% slope (silver paint), and up to 25% slope (nail polish)), with the highest degree of ease of mounting devices. Thus, PDMS was selected as the mounting adhesive for all future experiments.

c) Effect of scan speed and laser power

Observations:

When bubbling happens, the most natural idea one may come up with is to reduce laser power to reduce thermal accumulation within the resist and the structure. However, we were not able to build test structures without bubbles within the laser power range (5%-120% laser power) using nail polish and the default scanning speed of 100,000 um/s. For most samples, we could see burnt SIROF, whose texture significantly differs from normal SIROF, as shown in Figure 11.

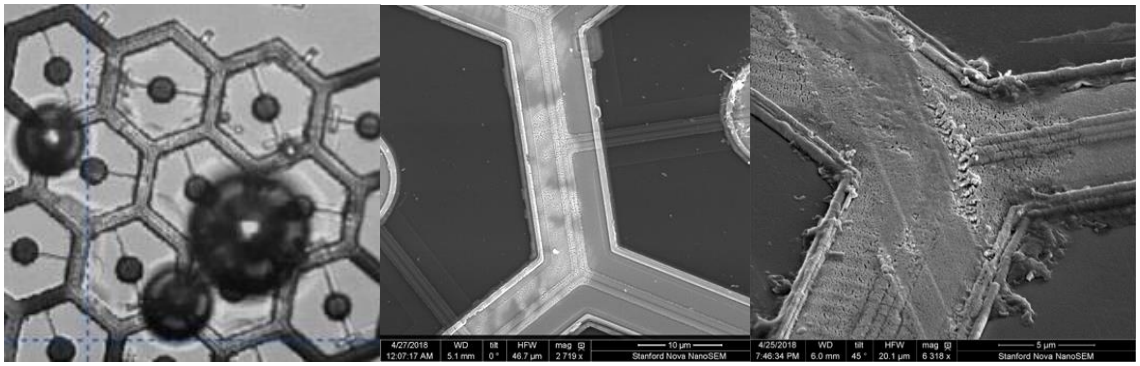

Figure 11. (a) example of bubbling appearing immediately following exposure. **(b, c)** examples of effect of bubbling on the SIROF substrate

Since we hypothesize that overheating is the major issue of building structures on SIROF, choosing the right adhesive (PDMS) is of high importance. We began to get some structures using PDMS, but still with terribly large bubbling holes. Beyond that, further suppressing overheating effect is not as simple as minimizing the power input per unit area. Examples are shown in the following comparisons.

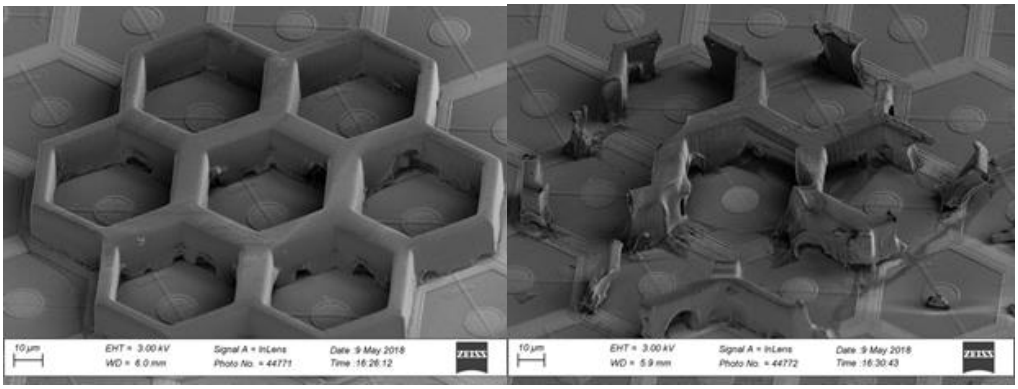

Figure 12. Both structures are built with PDMS adhesive, using hatching distance = slicing distance = 0.3 um, **(a)** Power = 30%, scanning speed = 2500 um/s; **(b)** Power = 100%, scanning speed = 100,000 um/s

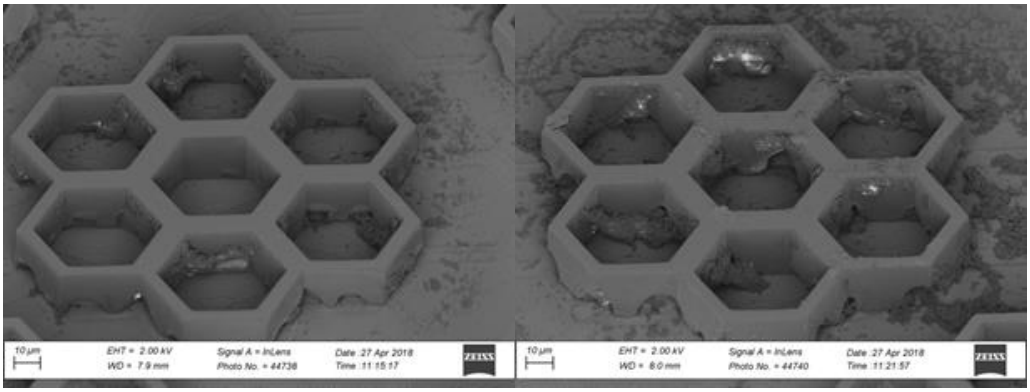

Figure 13. Both structures are built with silver paint adhesive, using hatching distance = 0.5 μm, slicing distance = 1 μm, power = 30%, **(a)** scanning speed = 1000 μm/s; **(b)** scanning speed = 2000 μm/s.

Power injection of the structure in Fig 12 (a) is 12 times higher than Fig 12 (b), yet Fig 12 (b) suffers from much more severe bubbling effect. Figure 13 gives a more direct comparison by showing that, with all other conditions held constant, a 2x increment of scanning speed (equivalently, 2-fold decrement of power injection) actually worsens the bubbling effect. So far, the optimal parameter configuration we have found is shown in Figure 14.

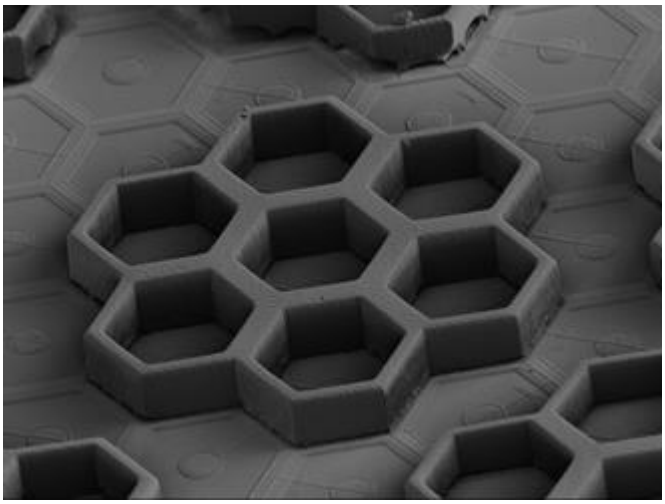

Figure 14. Structure built with the optimal configuration: adhesive = PDMS, laser power = 15%, scanning speeding = 250 um/s, hatching distance = slicing distance = 0.8μm.

To elaborate upon the nonlinearity of the dependence on injected energy on bubbling, we show in Figure 15 the parameter space explored. Figure 15(b) graphically shows the decreasing scan speed or decreasing power does not always result in minimizing the bubbling phenomenon.

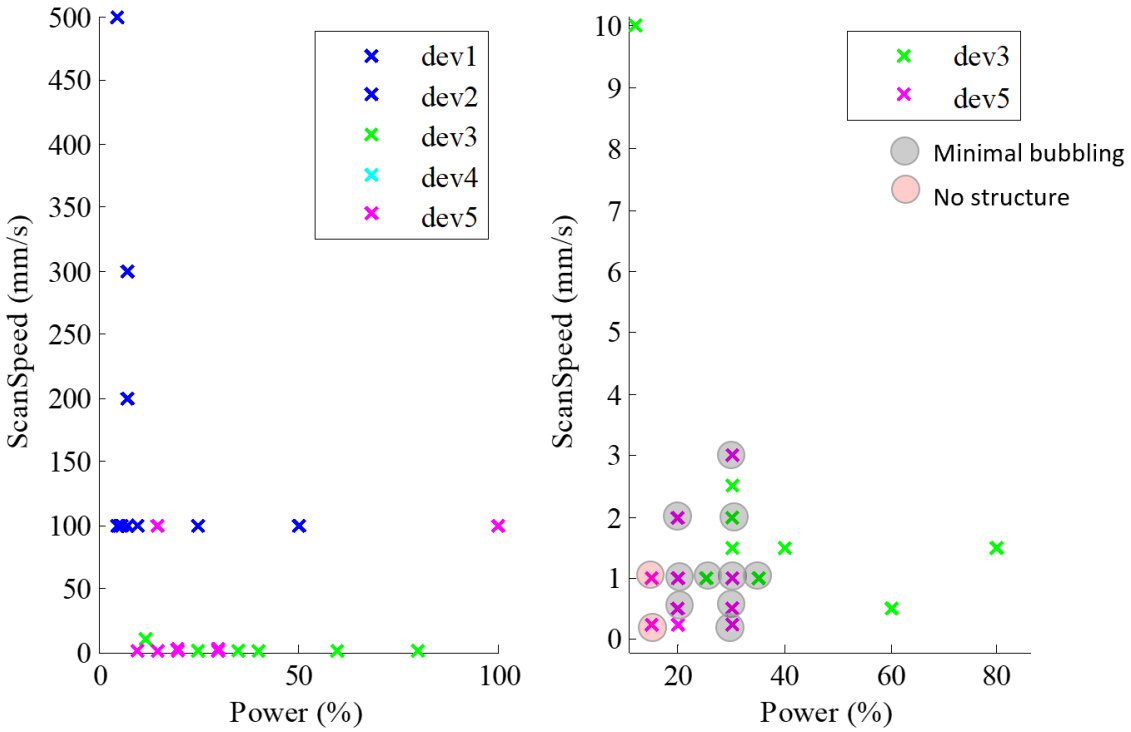

Figure 15. (a) Graphical illustration of tested combinations of scan speed and power. The legend indicates the different devices used. Devices 1-2 were mounted with nail polish, Device 3 was mounted with silver paint, and Devices 4-5 were mounted with PDMS. **(b)** Subplot of **(a)**.

d) Hypothesis

Since the substrate we use is very non-standard, it is hard to draw any quantitative conclusion regarding thermal effect. Nevertheless, based on the observations above, we raise the following hypothesis to explain what we observed and to guide future parameter tuning.

The amount of bubbling is modulated by the heat diffusion coefficient of the substrate. Beyond that, we propose that the relative relationship between lateral and vertical diffusions determines the characteristics of overheating, which can be categorized into one of the following three modes:

I. *Local heating:* overheating happens primarily around the laser spot. This happens when vertical diffusion is significantly better than the lateral;

II. *Regional heating:* overheating happens primarily within several hatching lines from the one being written. The heat cumulation from several neighboring "hot lines" causes bubbling. This happens when vertical and lateral diffusion coefficients are similar;

III. *Global heating:* overheating happens all over the device simultaneously. This happens when vertical diffusion is significantly worse than the lateral.

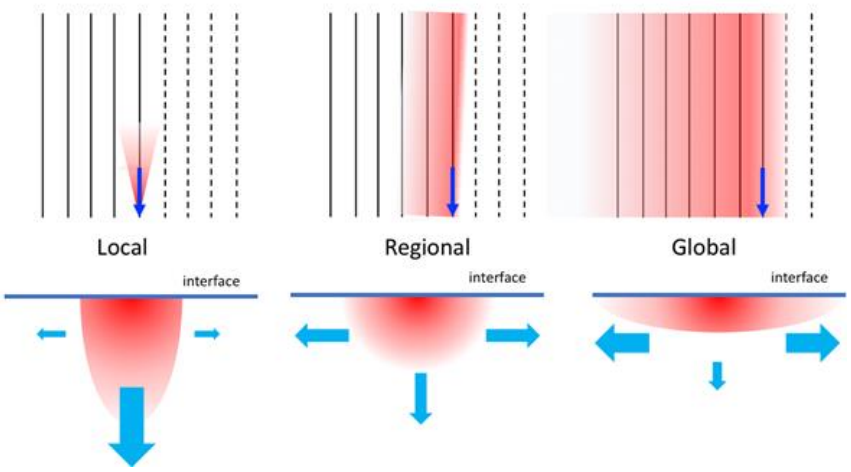

Figure 18: Different modes of heating effect. Solid black lines are the written trajectory, while dashed black ones are yet to write. Blue arrows show the moving directions of laser beams. Cyan arrows represent heat diffusions, each of which is proportional to the thickness of the arrow.

The three different modes have very different implications for parameter tuning, although in all cases lower laser power is always more preferable for suppression of bubble formation. For the local heating mode, faster scanning speed is preferable since power injection per unit area is lower. However, for regional heating faster scanning speed means more bubbling, as the time difference between each two neighboring hot lines is too short for heat to adequately disperse. In this case, increasing hatching distance and slowing down scanning speed is desirable. If global heating dominates, increase of hatching distance is beneficial because of the reduced total energy injection. When hatching distance is increased, it is advisable to decrease slicing distance for the structure's integrity. The following table summarize the characteristics of different modes and their respective parameter tuning direction.

Mode		Local	Regional	Global
Dominant cause		Laser point overheats	A few neighboring lines overheat	Whole substrate overheats
Lateral Diff.		Relatively slow	Similar to vertical	Relatively fast
Vertical Diff.		Relatively fast	Similar to lateral	Relatively slow
Parameter tuning direction	Laser power	Down	Down	Down
	Scanning speed	Up	Down	Not relevant

	Hatching Dist.	Not relevant	Up	Up
	Slicing Dist.	Not relevant	Down	Down

In our case, because the optimal scanning speed is much lower than the default value, we are confident to eliminate the possibility of local heating. Our leading hypothesis is that regional heating is the dominant mode in our case. Since we have already found an acceptable configuration, we did not spend too much time to differentiate between the regional and global modes. The following experiment would potentially validate this model and determine the dominant mode for bubbling:

On a large substrate, a series of cuboid structures are written. All structures share the same parameters expect for scanning speed and hatching distance. Scanning speed and hatching distance vary while the product of them stays constant for each structure. In this way, we control the total energy injection and total writing time. If global heating is the dominant mode, no significant difference is expected among the structures. Otherwise, if fast scanning speed and short hatching distance extensively increase bubbling, it proves that regional heating dominates.

III. Resist molds

In the resist molds section of the project, the goal is to achieve high-aspect ratio structures for subsequent electroplating. With conventional exposure methods such as stepper lithography (ASML), the numerical aperture prevents high aspect ratio structures with smooth, straight sidewalls. Hence, three-dimensional lithographic methods offer promise in achieving high aspect ratio structures. These structures need to have (1) smooth sidewalls, (2) cover a vertical span of 25 um (the thickness of the spray-coated resist), and (3) possess satisfactory structural integrity and quality.

Fabricating resist molds involves a series of steps. We begin with a silicon wafer coated with 100 nm platinum on a 20 nm titanium adhesion layer. We prime this wafer with hexamethyldisilazane (HMDS) using svgcoat2, and spraycoat 25 passes of resist (7.5% SPR220-7, 68% MEK, 24.5% PGMEA). This wafer is then baked on a hotplate at 90 C for 5 min and experiences a rest time of 3 or more hours before exposure. Post-exposure, the wafer is developed in MF-26A for 3.5 min and descummed in oxygen plasma for 1 min.

a) Exposure of thick resists

Initial conditions revealed that the incomplete exposure all the way through the resist, as shown in Figure 19 However, the edges are quite smooth, which fulfills one of our criteria.

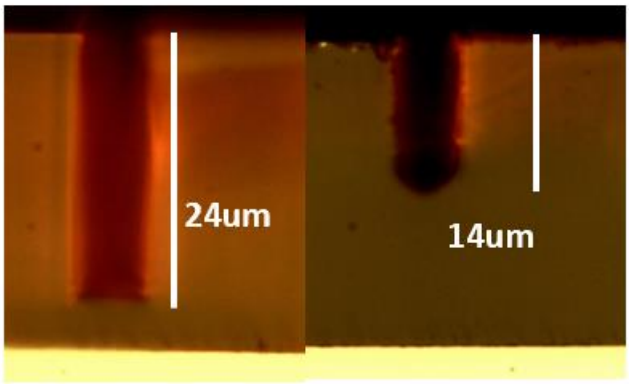

Figure 19. Cross-section microscopy images of exposed honeycombs in the resist.

We attempted a dose matrix to fix the above issue and polymerize all the way down the resist. An exposure matrix for both the 25 µm and 4 µm resists was produced, in which speed and interface position were varied. We wrote structures at the standard hatching distance of 0.5 µm, slicing distance of 1 µm, and power of 100%. For 25 µm of spray-coated resist, we used interface positions of 0.5, 1, 2, 4, 6, 8, and 10 µm below wherever the interface finder determined as the starting plane. Below is an explanation of how the interface finder works:

a. The interface position command determines where the Nanoscribe starts writing from. First, the interface *finder* attempts to find a reflection for 830 nm light incident on the resist. If the thickness of the resist is smaller than the vertical resolution commensurate with the objective used, then the software will have a difficult time differentiating between the air/resist and resist/substrate interfaces. In most cases, the system will position the laser focus somewhere in between the two interfaces, which is why the interface position command may be necessary to force the system to move the focus closer to the resist/substrate interface. Higher magnification objectives offer better resolution for the interface finder, since the depth of focus is lower and thus the system can more easily distinguish one interface from the other for a sufficiently large distance between the air/resist and resist/substrate interfaces.
b. The interface finder relies upon a sufficient index contrast between the substrate and the resist so that a back-reflection can be detected. However, if this index contrast is too great, a standing wave pattern could be formed, causing reflections that can not only influence the interface finder reading but also the exposure dosage during writing.

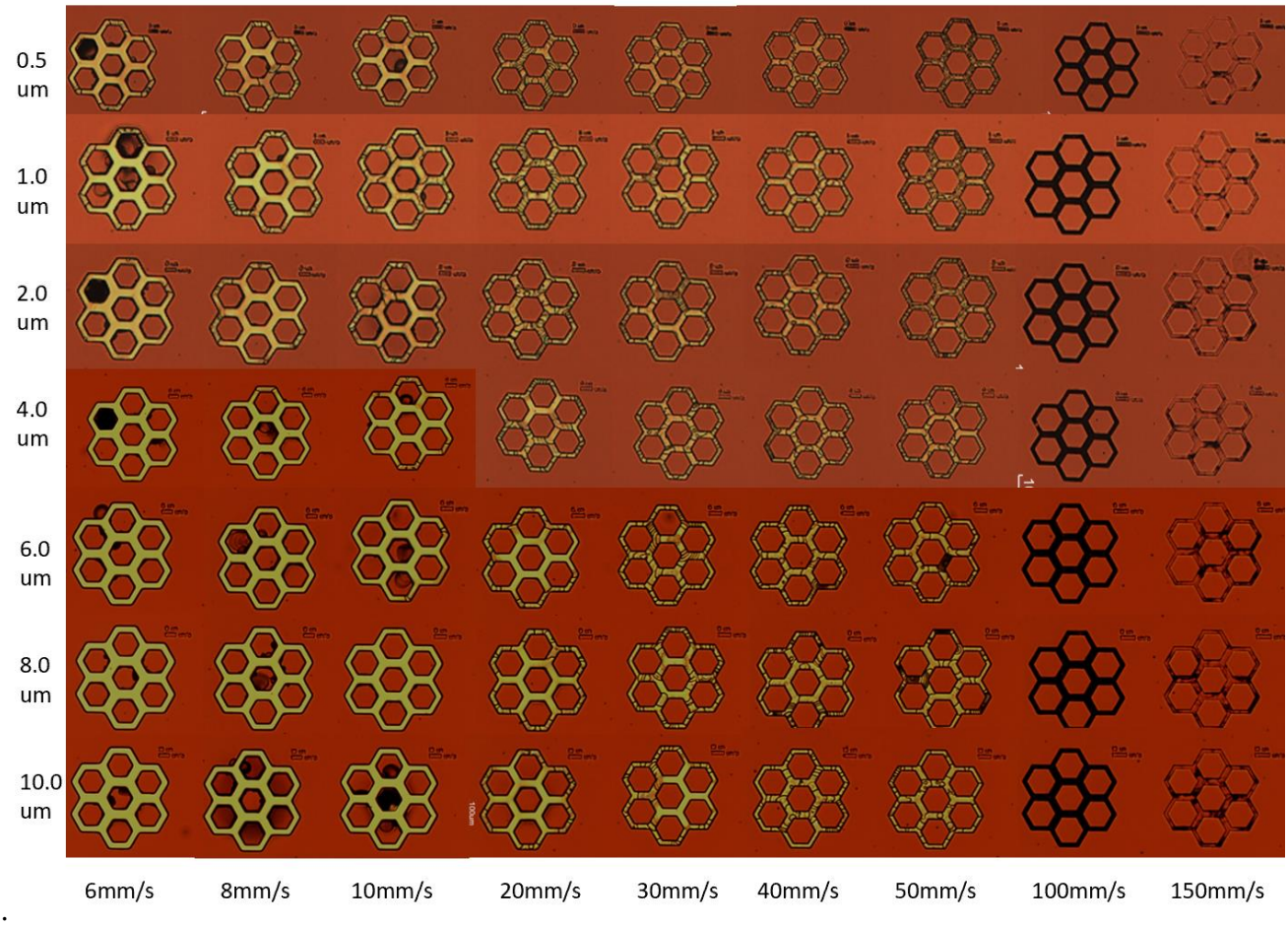

Figure 20. Exposure matrix varying interface position and scan speed.

From Figure 20, we see that slower speed offer higher doses, and thus results in a clearer pattern. More surprisingly, lower interface positions offered clearer patterns. As the speed is increased or the interface position not placed low enough, the resist does not polymerize fully and hence becomes less visible even after vigorous development.

A few explanations exist for why deep interface position offer clear patterns. One reason is that the Nanoscribe may be having a hard time finding the interface, because the resist is *too* thick, and the index contrast between the resist (~1.62 at 830 nm) and substrate (Si, 3.6 at 830 nm) is *too* large. According to Nanoscribe instructions, near the vicinity of the surface of the the highly reflective substrate (e.g. silicon) standing wave patterns may be seen due to back-reflections from the incident Gaussian beam. Hence, this confuses the interface finding system, and forces it to find an average between where these reflections occur and where the position of the reflection at the first interface (air/resist) occurs, producing an erroneous starting interface for the writing procedure. A computation of the Rayleigh length of the objective at the wavelength in question allows one to obtain a rough estimate of the depth of focus (DOF) of the Gaussian beam. The spot diameter, which is the diameter of the Gaussian beam at the waist (at the focus), is roughly

$$D = 1.22\,\lambda/NA$$

where NA is the numerical aperture of the objective and λ the wavelength (note, we assume the Paraxial approximation here, which normally works for low NA, but surprisingly converges well to physical optical results if a factor of two is accounted for). The Rayleigh length for a Gaussian beam is given by

$$z_R = \pi {w_0}^2/\lambda$$

where w_0 is the beam waist or half-diameter. For the interface finder wavelength of 830 nm and a 25x objective with NA of 0.8, we compute a Rayleigh length of ~1.34 μm. This is much smaller than the thickness of the resist, so DOF is not an issue here, and the two interfaces are far enough away that they can be distinguished as the piezo-motor mechanically moves the objectives to and fro the two interfaces.

Thermal heating issues are less serious for this part of the project due to the thermal robustness of silicon as compared to SIROF; however, it is important to note that when the interface position is placed lower into the resist, and eventually into the substrate, a virtual focus of the input Gaussian beam is set in the substrate, which is how most of the optical power is dissipated in the substrate rather than this resist. This causes local heating, because a good portion of this power is absorbed by the silicon (830 nm light, ~0.8E+03/cm absorption), although some is reflected back into the substrate. This local heating may change the sensitivity of the resist to the exposure dose.

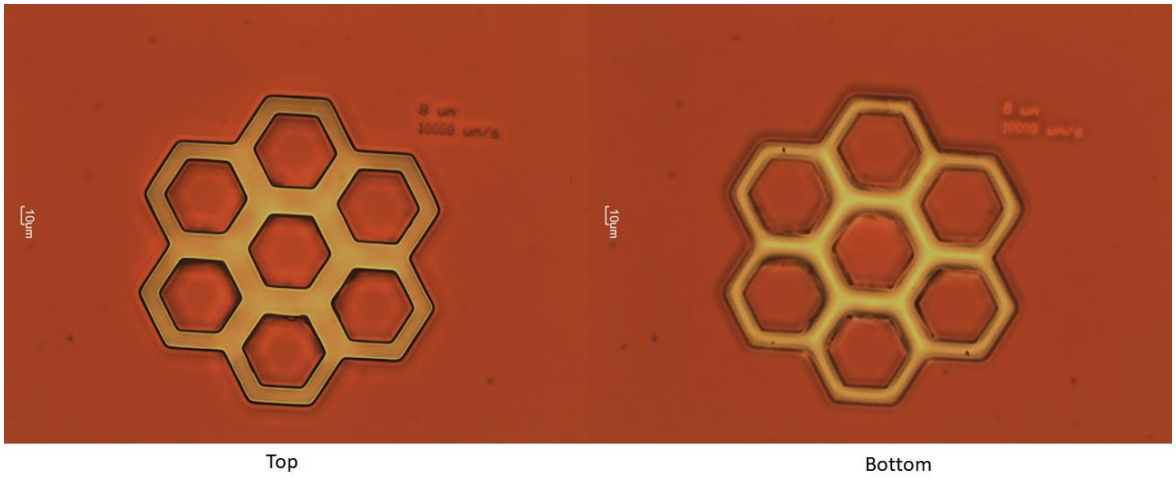

Figure 21. Microscope images focused at the top and bottom of the resist mold at the optimal exposure condition.

Figure 21 shows the best structures from the study. At an interface of 8 μm below the interface finder position and speed of 10 mm/s, both the top and bottom interfaces of the structure appear to be fully developed. There is a balance between the speed and interface setting for optimal writing, though it appears the speed (which is directly proportional to the dose) is most influential in this study. If the dose is too high, then the features become larger than desired, not to mention the longer write times, which will ultimately come into play once the larger full-device structures are written. Moreover, we see that at lower speeds (higher dose), the presence of black spots in the hexagonal features above suggests damage to the silicon.

This study was repeated also for 4 μm resist thickness, because these thinner resists are easier and faster to deposit; moreover, since we confirmed the straightness of the high-aspect ratio structures in the 25 μm resist, going to 4 um would not make a difference in the other experimental studies we would make, namely, the alignment study (discussed later).

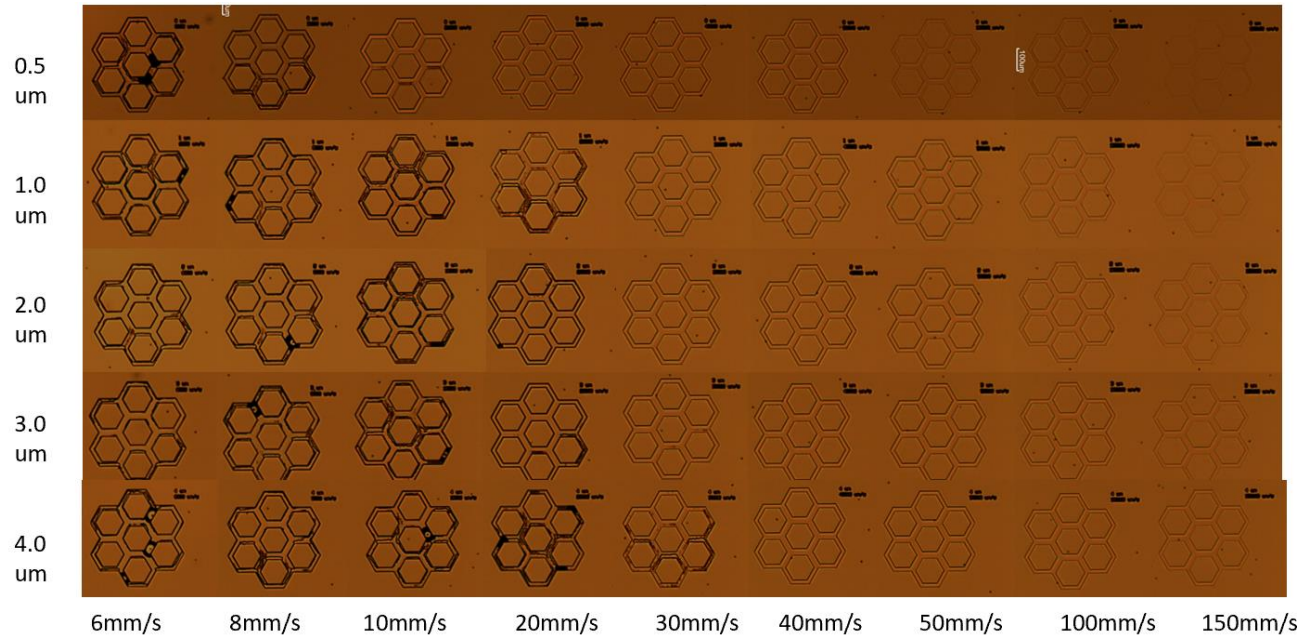

Figure 22. The trend is confirmed also for the 4 um resist matrix.

b) Large-scale two-photon lithography

Several issues must be considered with full -wafer scale lithography. The major issue is whether two-photon polymerization (TPP) is fast enough to do full wafer-scale lithography and the constraints involved for efficient large-scale lithography. Related to this is the issue of alignment and whether the system has adequate alignment across a large scale.

Speed

As TPP is essentially a 3D printing technology like laser sintering, several of the same considerations which apply to 3D printing technologies apply to TPP as well. It offers impressive resolution (< 100 nm), but, like other high-resolution serial lithography techniques (e-beam), is criticized for the long writing time. TPP generally takes in the range of a few seconds to several days to write a structure. The time it takes is dependent on two parameters: the speed and linear distance to be traversed [13,21].

We used Describe software to approximate writing times for our hexagonal array (Figure 23a). We first varied scan speed from 100,0000 um/s to 10,0000 um/s. Decreasing the scan speed by 10 caused a 36% decrease in throughput, while decreasing the slicing distance caused a 44% decrease in throughput, and decreasing the hatching distance by 2 caused a 48% decrease in throughput. From these trends, we recommend decreasing the scan speed rather than decreasing hatching or slicing distance in order to achieve a clearing dosage in minimal time. While we didn't explore the effects of blocking, reports indicates that increasing the block size may decrease write time as well.

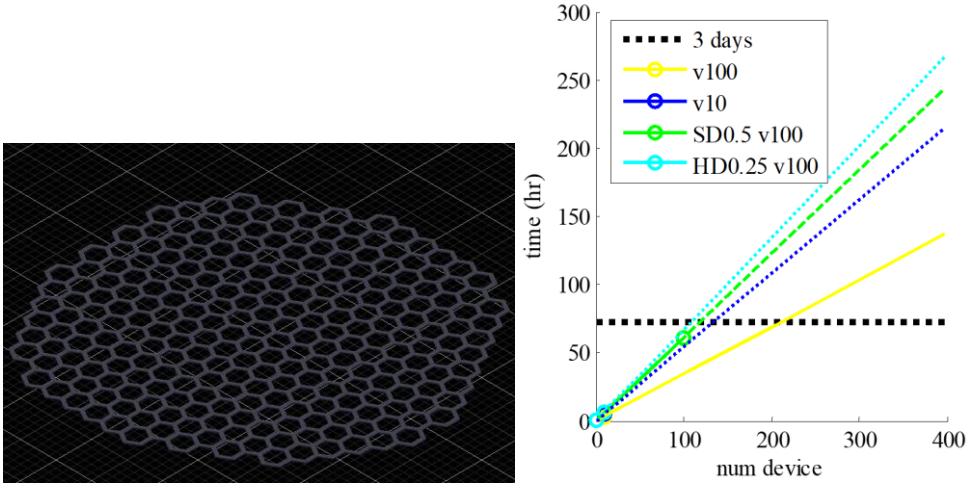

Figure 23. (a) Structure considered for optimizing parameters to decrease time. This is a 1 mm in diameter structure composed of 55um wide hexagons with 11 um wide walls. It is 1 um thick. **(b)** Effect of printing parameters on time to write structure.

Alignment

Alignment in a serial system like two-photon lithography is less related to the inherent ability of the machine or the user to align a mask to the entire pattern (a la *ASML, Karlsuss*), but rather, the inherent error of the stage motor dominates. To avoid this issue, it is possible to align a pattern multiple times across a wafer, but we would prefer to reduce the amount of manual alignment necessary as this can be quite time-prohibitive. To measure the error in this stage, we patterned crosses across the wafer in metal (Figure 24), manually aligned to the leftmost and rightmost cross in Nanoscribe, and patterned crosses on top of the existing crosses. The crosses are located 5 mm apart.

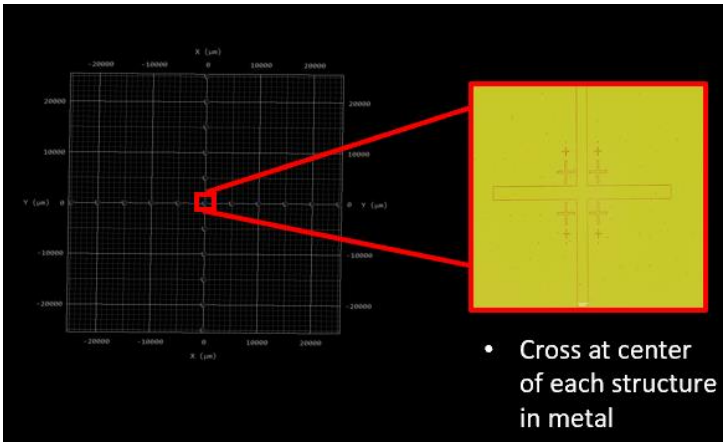

Figure 24. Diagram of Nanoscribe exposure pattern. Each cross is located 5mm apart.

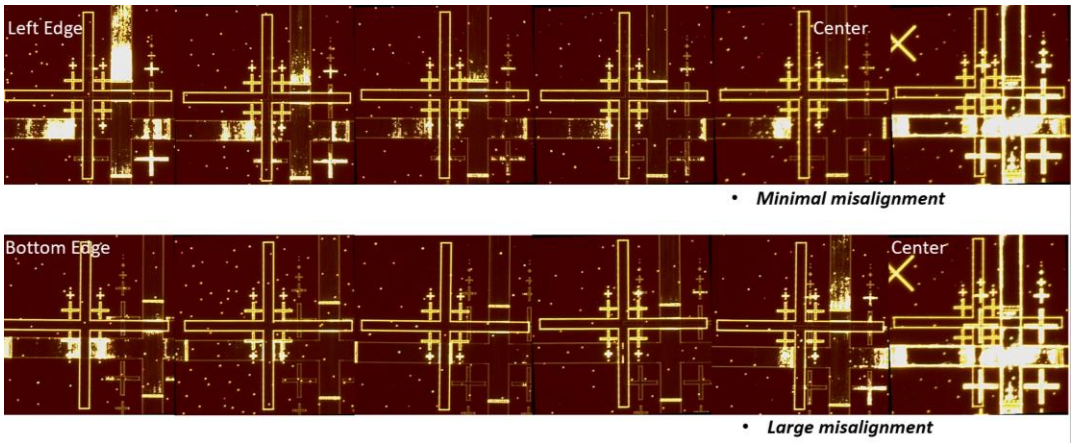

Figure 25. Microscope images of crosses exposed by Nanoscribe aligned to crosses exposed by Heidelberg. The leftmost image is closest to the edge of the wafer and the rightmost image is the image at the center of the wafer. The top row is in the horizontal direction, and the bottom row is in the vertical direction.

	Edge					Center
X-Dir [um]	<3	<3	<3	<3	<3	N/A
Y-Dir [um]	85	60	45	25	10	N/A

Figure 26. Measurements of misalignment between the metal and the Nanoscribe crosses

From these measurements, we see that there is minimal stage error in the horizontal direction. However, in the vertical direction, the error is on the order of 10-90 um. Note: future studies should use vernier marks for measuring alignment rather than crosses, and this study should be repeated for validation. This study shows that the Nanoscribe system at Stanford achieves more accurate alignment along the horizontal axis than along the vertical axis.

IV. Conclusion

To further the fabrication goals of photovoltaic retinal prostheses with honeycomb walls, we have explored considerations involved in fabricating both resist structures on non-standard substrates and resist molds in thick resists. We have optimized the process for attaching implants to a substrate by using a PDMS adhesive, studied the effect of speed and power on resist structures and optimized these parameters to limit bubbling, and hypothesized that this bubbling effect is related to heat. We have also optimized exposure conditions for thick spray-coated resist by adjusting the scan speed and interface position, and considered conditions for large-scale lithography, specifically considerations for speed and alignment. These results will enable us to proceed with fabrication of the next generation of retinal prostheses to achieve high visual acuity.

V. References

1. MS. Humayun, M. Prince, E. de Juan, Y. Barron, M. Maskowitz, IB Klock, and AH Milan, Invest Ophthamol Vis Sci. 40(1), 143-148 (1999).
2. A. Santos, M. Humayun, E. de Juan, RJ Greenberg, MJ Marsh, IB Klock, and AH Milan, Arch Ophthalmol 115(4), 511-515 (1997).
3. MR. Behrend, AK Ahuja, MS Humayun, RH Chow, and JD Weiland. IEEE Trans Neural syst Rehabil Eng, 19(4), 436-442 (2011).

4. D. Nanduri, I. Fine, A. Horsager, GM Boynton, MS Humayun, RJ Greenverg, JD Weiland, Invest Opthalmol Vis Sci. 53(1), 205-214 (2012)
5. K. Stingl, K Bartz-Schmidt, F. Gekeler, A. Kusneyrik, H. Sachs, and E. Zrenner, Invest Opthalmol Vis. sci 54(12), 7658-7665 (2013).
6. RJ Jenson, and JF Rizzo. Exp. Eye. Res 83(2), 367-373 (2006).
7. BW Jones and RE Marc. Exp Eye Res. 81(2), 123-137 (2005).
8. MS. Humayun, JD Dorn, L. da Cruz, G. Dagnelie, JA Sahel, Cideciyan S., JL. Duncan, D. Eliott, E. Filley, AC Ho, A. Santos, AB Safran, A. Arditi, LV Del Priorie, and RJ Greenberg, Opthamalogy 119(4), 779-788 (2012).
9. X. Zhau, Y. Hau, and J. Lin, AIP Advances 5, (2015).
10. T. W. Lim, S. H. Park, and D. Y. Yang, Microelectronic Engineering 77(3-4), 382-388 (2005).
11. K. S. Lee, R. H. Kim, D. Y. Yang, and S. H. Park, Progress in Polymer Science 33(6), 631-681 (2008).
12. J. Fischer, J. B. Mueller, J. Kaschke, T. Wolf, A. N. Unterreiner, and M. Wegener, Opt. Express 21, 26244-26260 (2013).
13. M. Malinauskas, M. Farsari, A. Pskarskas, and S. Juodkazis. Physics Reports 533 (1) 1-31 (2016).
14. T. Asavei, T. Nieminen, N. Heckenberg, and H. R. Dunlop, Journal of Optics A, 11(7) (2009).
15. T. Buckmann, N. Stenger, M. Kadic, J. Kaschke, A. Frolich, T. Kennerknecht, C. Eberl, M. Theil, and M. Wegener, Adv. Mater., 24, 2710-2714 (2012).
16. M. Vaezi, H. Seltz, and S. Yang, Int J. Adv Manuf. Technol. 67, 1721-1754 (2013).
17. Nanoscribe Photonics Professional (GT): User Manual. 23 October 2017.
18. D. Tan, K. N. Sharafudeen, Y. Yue, and J. Qiu. Progress in Materials Science 76 154-228 (2016).
19. F. Luo, G. Lin, H. Sun, G. Zhang, L. Liu, D. Chen, Q. Chen, Q. Zhao, J. Qiu, and Z. Xu. Optics Communications 284 (19) 4592-4595 (2011).
20. Y. Bellouard, and M.O. Hongler. Optics Express 19 (7) 6807-6821 (2011).
21. C. N. LaFratta, L. Li. Micro and Nano Technologies 221-241 (2016).
22. M. Malinauskas, M. Farsari, A. Pskarskas, and S. Juodkazis. Physics Reports 533 (1) 1-31 (2016).